AGU PUBLICATIONS

JGR

Journal of Geophysical Research: Solid Earth

RESEARCH ARTICLE
10.1002/2017JB015017

Special Section:
Stress, Strain and Mass Changes at Volcanoes

Seismicity in the Vicinity of the Tristan Da Cunha Hot Spot: Particular Plate Tectonics and Mantle Plume Presence

Antje Schlömer[1], Wolfram H. Geissler[1], Wilfried Jokat[1,2], and Marion Jegen[3]

[1]Alfred Wegener Institute, Helmholtz Centre for Polar andMarine Research, Bremerhaven, Germany, [2]Geoscience Department, University of Bremen, Bremen, Germany, [3]GEOMAR, Helmholtz Centre for Ocean Research Kiel, Kiel, Germany

Key Points:
- A temporary network of ocean-bottom seismometers and land stations is used to present the local seismicity around the volcanic island Tristan da Cunha
- Oceanic intraplate seismicity is associated to plate tectonic processes and the existence of the Tristan da Cunha mantle plume
- Seismicity close to the island and nearby seamounts is related to ongoing tectonomagmatic activity

Supporting Information:
- Supporting Information S1
- Table S1

Correspondence to:
A. Schlömer,
antje.schloemer@awi.de

Citation:
Schlömer, A., Geissler, W. H., Jokat, W., & Jegen, M. (2017). Seismicity in the vicinity of the Tristan da Cunha hot spot: Particular plate tectonics and mantle plume presence. *Journal of Geophysical Research: Solid Earth*, *122*. https://doi.org/10.1002/2017JB015017

Received 25 SEP 2017
Accepted 8 DEC 2017
Accepted article online 13 DEC 2017

Abstract Earthquake locations along the southern Mid-Atlantic Ridge have large uncertainties due to the sparse distribution of permanent seismological stations in and around the South Atlantic Ocean. Most of the earthquakes are associated with plate tectonic processes related to the formation of new oceanic lithosphere, as they are located close to the ridge axis or in the immediate vicinity of transform faults. A local seismological network of ocean-bottom seismometers and land stations on and around the archipelago of Tristan da Cunha allowed for the first time a local earthquake survey for 1 year. We relate intraplate seismicity within the African oceanic plate segment north of the island partly to extensional stresses induced by a bordering large transform fault and to the existence of the Tristan mantle plume. The temporal propagation of earthquakes within the segment reflects the prevailing stress field. The strong extensional stresses in addition with the plume weaken the lithosphere and might hint at an incipient ridge jump. An apparently aseismic zone coincides with the proposed location of the Tristan conduit in the upper mantle southwest of the islands. The margins of this zone describe the transition between the ductile and the surrounding brittle regime. Moreover, we observe seismicity close to the islands of Tristan da Cunha and nearby seamounts, which we relate to ongoing tectono-magmatic activity.

1. Introduction

Tristan da Cunha (TdC) is a small volcanic island in the South Atlantic Ocean that belongs to the eponymous archipelago (Figure 1). Besides the inhabited main island, the archipelago comprises the uninhabited Nightingale Islands, the wildlife reserve Inaccessible Island, and a number of smaller islands.

TdC is situated at the southwestern end of the Walvis Ridge-Tristan/Gough hot spot track, 450 km east of the present-day axis of the Mid-Atlantic Ridge (MAR). Currently, different hypotheses exist to explain the geodynamic evolution of this island: The origin of TdC is either attributed to shallow plate tectonics (e.g., Anderson & Schramm, 2005) or to the existence of a mantle plume (e.g., Courtillot et al., 2003; Morgan, 1971; White & McKenzie, 1989). It has long been accepted that melts derived from a mantle plume directly beneath the island formed the archipelago (O'Connor & Duncan, 1990; Rohde et al., 2013). Schlömer et al. (2017) recently imaged a plume conduit southwest of TdC by calculating a *P* wave tomography with data registered by the seismological network also used for this study. Their study also proposed that hot plume material is currently being channeled along the base of the lithosphere toward the islands and nearby seamounts.

The slow-spreading southern MAR is strongly segmented by transform faults that continue as fracture zones into the surrounding plate interiors. A ridge crest offset of 250 km is observed at a large transform fault north of TdC (Figure 1, Northern Transform Fault, NTF). This offset is among the largest in the South Atlantic Ocean. Directly south of the archipelago, a 25 km offset forms the transform fault section of the Tristan da Cunha Fracture Zone (Figure 1, TdCFZ).

Very little is known about local and regional seismicity because of the remote location of the study area and sparse seismometer coverage in and around the South Atlantic. Only a few studies have investigated the seismicity at the archipelago or in its vicinity. Baker et al. (1962) reported on the most recent onshore eruption, which occurred in 1961 close to the capital settlement of TdC and was accompanied by seismic

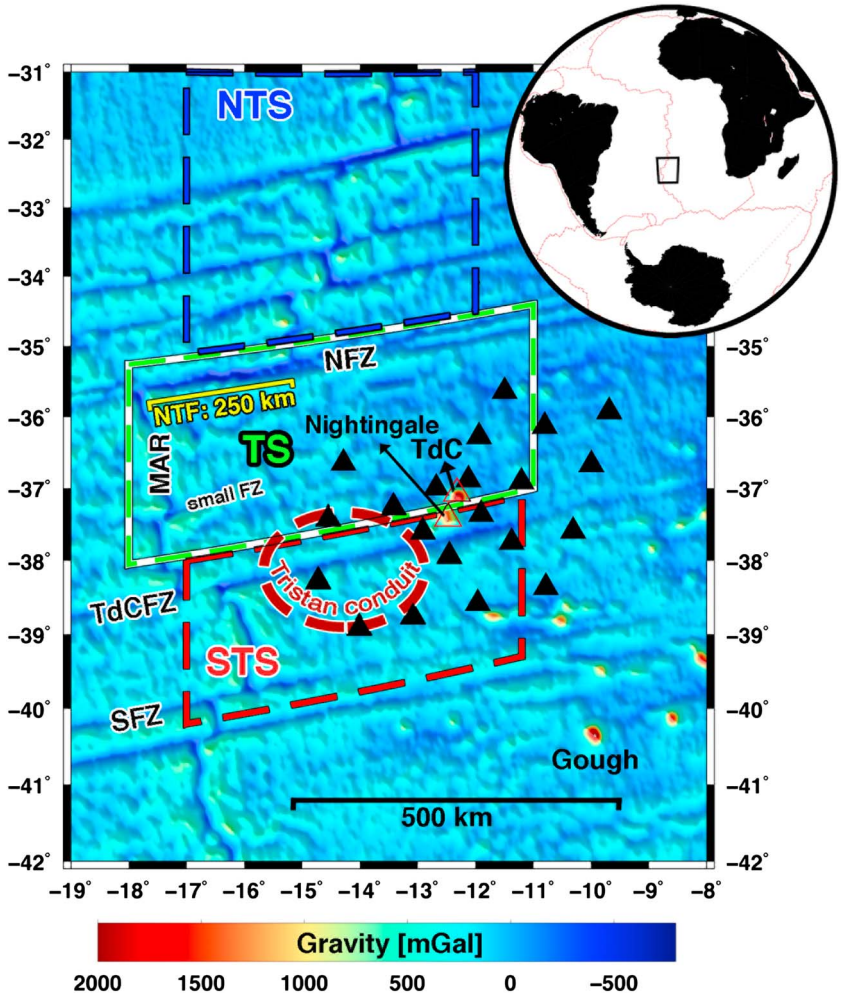

Figure 1. Satellite gravity map (Sandwell et al., 2014) of the study area, including locations of OBS (black triangles) and land stations (Nightingale and TdC: red framed triangles). The study area is divided into a Northern Tristan Segment (NTS), a Tristan Segment (TS), and a Southern Tristan Segment (STS). The discussed fracture zones are the Northern Fracture Zone (NFZ), a small Fracture Zone (small FZ), the Tristan da Cunha Fracture Zone (TdCFZ), and the Southern Fracture Zone (SFZ). The Northern Transform Fault (NTF), the Mid-Atlantic Ridge (MAR), and the location of the Tristan conduit found by *P* wave tomography (after Schlömer et al., 2017) (red dashed ellipsoid) are also marked. The inset map shows the study area (black framed) and the main plate boundaries (red).

activity. The Tristanians felt further earthquakes in 2004. Hards (2004) associated the pumice found on the beaches of TdC and on the sea surface to a submarine vent on the flanks of the Tristan volcano. Using data from two hydroacoustic stations, O'Mongain et al. (2007) located a swarm of earthquakes close to Nightingale Island, probably as a consequence of the large 2004 earthquake. Haxel and Dziak (2005) detected seismicity along the older part of the Walvis Ridge northeast of our study area and explained the occurrence of earthquakes in terms of the recurrence of magmatic activity there. The global network catalog (NEIC, National Earthquake Information Center) of the United States Geological Survey only provides events with magnitudes (MB) larger than 4 and considerable location uncertainties due to great distances to the recording stations. These global catalog earthquake locations are insufficient to investigate the local seismicity at this remote archipelago.

Here we use a temporary network of ocean-bottom seismometers (OBS) and island stations to present a novel study of local seismicity around the island of TdC. Our results give new insights into oceanic intraplate seismicity, the role of mid-ocean ridges and transform faults, mantle plumes and their potential interaction, and tectono-magmatic processes. The close proximity to the MAR, the Tristan mantle plume, and a large

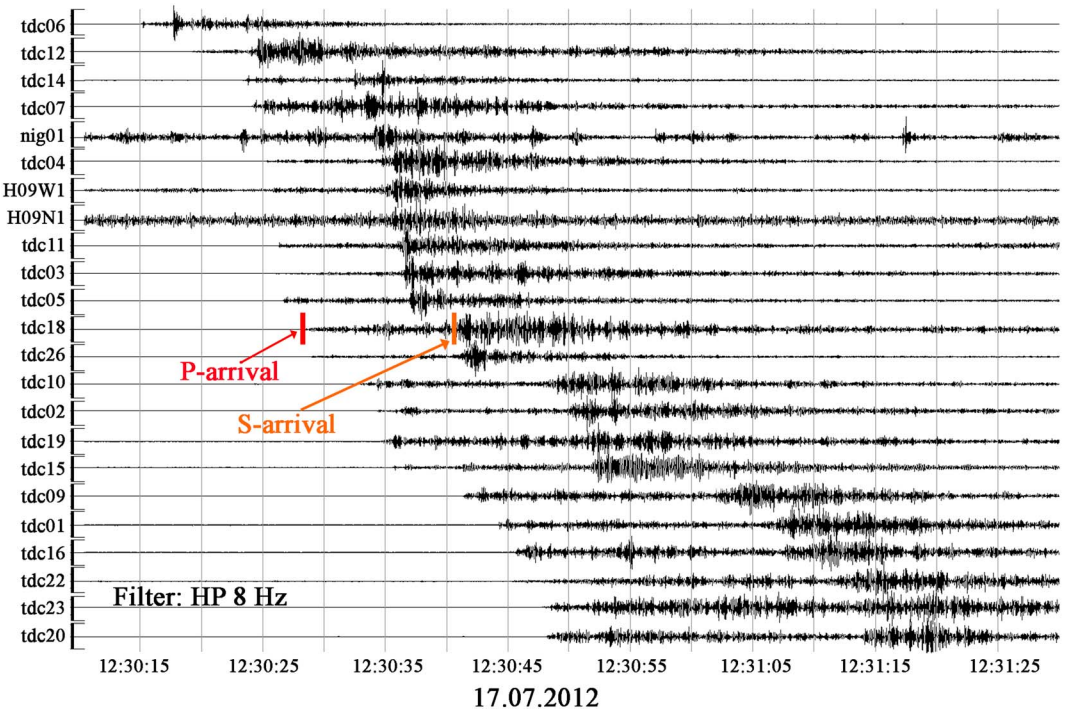

Figure 2. Example of a local earthquake occurred within the network close to the archipelago of TdC (37.69°S, 11.50°W). The waveforms are sorted with increasing distances from receivers to the earthquake. The figure shows high-pass filtered (8 Hz) vertical seismometer recordings. Origin time: 17.07.2012 12:30:11 UTC.

transform fault in the study area make TdC to a location with a unique geodynamic setting and therefore prevent a direct comparison with other regions.

2. Data

We deployed a network consisting of 24 ocean-bottom seismometers (OBS) and two land stations around and on the island of TdC and on Nightingale Island, during the RV *Maria S. Merian* cruise MSM 20/2 (January 2012). The network covered an area of 400 km × 500 km with TdC in its center and its western boundary 120 km east of the MAR (Figure 1). The average station spacing was approximately 85 km. All land stations and OBSs were equipped with a three-component seismometer (Guralp-3ESP Compact 60s and Guralp CMG-40 T 60s). The OBS systems were also equipped with a hydrophone (HTI-01 100 s). The instruments recorded continuously seismological data for 1 year with a sampling frequency of 50 or 100 Hz and were recovered during the cruise MSM 24 (January 2013). Two OBS could not be recovered, and one OBS did not record any data. We extended our data set by adding data from the IRIS (Incorporated Research Institutions for Seismology) seismometer station TRIS (STS-2 120 s) and two hydroacoustic stations (Geotech S13 1 s), H09N1 and H09W1, operated by the CTBTO (Comprehensive Nuclear-Test-Ban Treaty), all located on the island of TdC. Unfortunately, the permanent seismometer station TRIS was flooded in early 2012 and thus only provided data for 2 weeks at the beginning of our experiment.

Figure 2 shows the vertical seismometer recordings for a local earthquake (Table S3 No. 427) located within the network, in close proximity to Nightingale Island. Distinct *P* wave and *S* wave arrivals can be observed in most seismograms. The signal-to-noise ratio is much smaller at the land stations (H09N1, H09W1, and nig01) in comparison to the OBS stations. This can also be observed in corresponding spectrograms of these stations (Figure S1 in the supporting information). TdC is located in a region of strong year-round westerly winds and thus subjected to a high noise level at frequencies around 1 Hz recorded in the OBS data (Figures S1a and S1b) and above 3 Hz recorded by the land stations (Figures S1c and S1d) as a result of winds and surf arriving at the islands' coast. Unfortunately, local earthquakes are usually strongest in the 1–10 Hz frequency band. Consequently, less than 1% of the picked arrival times was obtained from the land stations.

Table 1
P Wave and S Wave Velocity-Depth Model for the TdC Region

OBS stations				Island stations			
Layer	Depth (km)	V_P (km/s)	V_S (km/s)	Layer	Depth (km)	V_P (km/s)	V_S (km/s)
Sediment	4.2–5	2	1	1. Crust layer	−2–5	4.8	2.7
Crust	5–10	5.4	3.7	2. Crust layer	5–10	5.4	3.7
Mantle	> 10	7.9	4.5	Mantle	> 10	7.9	4.5

3. Methods

First, we applied linear time corrections for clock drifts (skews) of the OBS recorders. The skew values for most of the OBS ranged between 0.1 s and 1.5 s over 1 year (Figure S2). We also corrected the timing of the seismograms for a leap second that occurred in 2012. Afterward, we applied a short time average/long time average trigger algorithm to the continuous data set. Prior to this application, the data were high-pass filtered at frequencies above 8 Hz to reduce the wind- and ocean-induced noise. Above this frequency, the OBS signal of a local earthquake contains its highest energy (Figures S1a and S1b). In the filtered seismograms, the algorithm also identified acoustic signals emitted by marine mammals. Consequently, the overall detections served only to find potential local earthquakes in the recorded data set. Subsequently, the *P* wave and sometimes additionally *S* wave arrivals were manually picked. We used the hydrophone and vertical components to identify the *P* arrivals and the horizontal components to identify the *S* arrivals. Around 30% of the identified earthquakes were not used in our study because the seismograms were too noisy to identify a clear first arrival.

3.1. Earthquake Location

For earthquake location, we used the algorithm *dbgenloc* (Pavlis et al., 2004) implemented in the Boulder Real Time Technologies Antelope software and *P* arrivals of at least five stations. In the absence of information concerning the velocity structure of the crust beneath TdC, we calculated a Wadati diagram (Wadati & Oki, 1933) (Figure S3) to identify inhomogeneities in the crustal structure. The diagram, calculated with 461 *S* and *P* arrivals of 74 events, does not show significant differences along the transects and therefore indicates no appreciable variations in the crustal structure within the study area. The average compressional to shear wave velocity ratio is $\frac{V_P}{V_S} = 1.74$, which match the expected relation of $V_P \approx \sqrt{3} * V_S$ typical of oceanic crust. The coefficient of determination R^2 is calculated to be 0.996, which indicates small picking errors.

The software uses a one-dimensional velocity model to calculate traveltimes. Therefore, we assumed a homogeneous oceanic crust with an overlaying 800 m thick sediment layer for the OBS stations and a two-layered oceanic crust for the island stations. We derived the crustal *P* wave and *S* wave velocities from a seismic refraction velocity models across seamounts of the Walvis Ridge and across the Discovery seamount (42°S, 0°10.02′°E) (Jokat & Reents, 2016). These seamounts are located 1,500 km away from TdC but provide the only direct information on crustal velocities in this region. Furthermore, we assumed a Moho depth of 10 km (below sea level) for this region. This value is obtained by *Ps*-receiver functions (Geissler et al., 2016), calculated with data from this network. Table 1 and Figure 3 illustrate the used velocity-depth model. The location algorithm considers negative elevations for the OBS and treats them like borehole seismometers. Possible errors caused by the inadequately clarified crust velocities beneath the island are small on the basis of less than 1% arrival times derived from land stations.

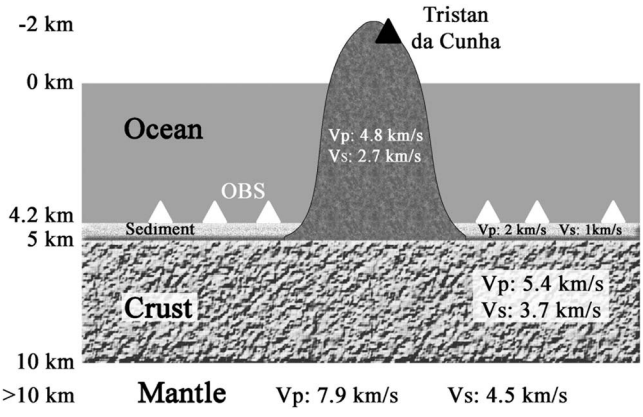

Figure 3. Schematic crustal velocity-depth model for OBSs located on the ocean floor and land stations located on the island of TdC.

We located the earthquakes with a fixed depth of 10 km. Clear *P* and *S* arrivals of 20 earthquakes within the network allowed the determination of hypocenter depths (Table S3). We were not able to identify any first motion polarities.

The location routine weighted individual observations by the inverse of the picking errors. We assumed a uniform error of 0.5 s. At the end of the location process, earthquakes with a root-mean-square (RMS) traveltime residual larger than 1 s were eliminated. A maximum

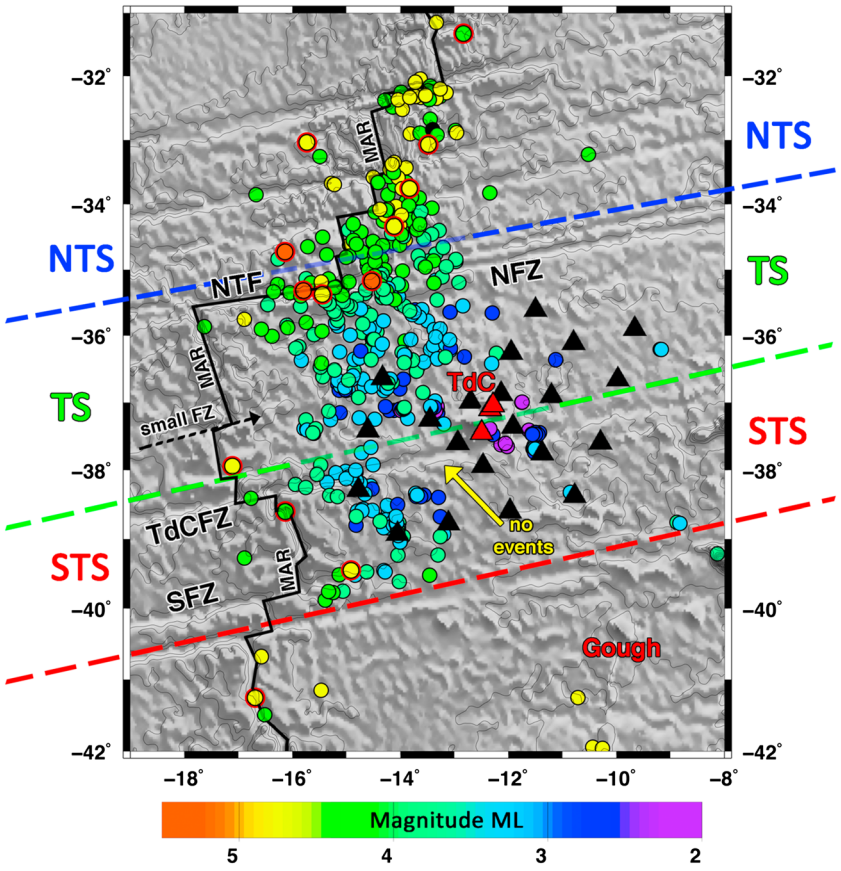

Figure 4. Spatial distribution of local earthquakes in 2012 (black framed circles). The color indicates the local magnitudes of the events. The red-framed circles are NEIC catalog events in 2012. A yellow arrow marks an aseismic zone southwest of TdC. The Abbreviations are listed in the caption of Figure 1.

measure of the epicentral error was determined by the length of the major and minor axis of the horizontal components of the confidence ellipse. The depth error for the hypocenter locations was estimated with the maximum value for the four principal axes of the confidence ellipsoid projected in the vertical direction. The uncertainty ellipsoids for 58% of the localized earthquakes have major axis lengths $\leq$ 10 km and those for 31% of the events have major axis lengths $\leq$ 30 km. Finally, we obtained 437 events from 4,076 *P* arrivals and 555 *S* arrivals (Tables S2 and S3).

3.2. Magnitude

We calculated the local magnitudes (ML) for all located events. First, the data were filtered with a Wood-Anderson Velocity filter, whereby the gain of the instrument response was considered to ensure reliable conversion from velocity to displacement. Afterward, we measured the maximum amplitude of the earthquake on the vertical component. The local magnitude for an event measured at one station was calculated by $ML = \log_{10}(A_{max}) + B(d)$, in which A_{max} is the maximum amplitude and $B(d)$ is the Richter correction value, a function of the source-receiver distance. An amplitude value was eliminated if the signal-to-noise ratio of the measurement was below a given threshold. Abnormal magnitudes and outliers were also recognized and excluded. In a further step, we calculated the median value of all station magnitudes for each event. This value is not strongly affected by large outliers. The minimum local magnitude measured with the network was 2.0, and the maximum magnitude was 5.3, at distances of 64 km and 367 km to TdC, respectively.

4. Methods

4.1. Spatial Distribution of Earthquakes

Besides earthquakes along the MAR axis, transform faults and fracture zones, the overall spatial distribution of local events in the TdC region in 2012 (Figure 4) shows a high occurrence of intraplate

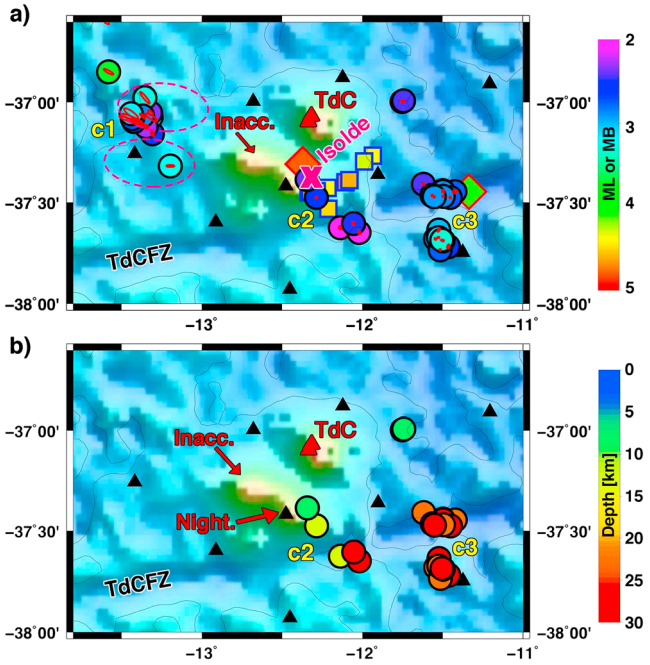

Figure 5. (a) Magnitudes of earthquakes. Black framed circles: our observations with error ellipses; red-framed diamond south of TdC: NEIC earthquakes (event time: 29.09.2013 09:27:38 UTC); red-framed diamond between Nightingale and TdC: NEIC earthquake (origin time: 29.07.2004 22:21:04 UTC); blue framed squares: swarm locations (after O'Mongain et al., 2007) (origin times: 29–30.07.2004); red dashed ellipses: volcanic fields (after Geissler et al., personal communication); magenta cross: location of newly discovered seamount Isolde (Geissler et al., personal communication). The color indicates the body wave magnitude for NEIC events and the local magnitudes for our events. The NEIC, swarm, and c1 earthquakes were localized with fixed depths. (b) Hypocenter locations of 2012 in two different clusters (c2 and c3). The color indicates the hypocenter depth. Abbreviations: TdC, Tristan da Cunha; Night, Nightingale Islands; Inacc., Inaccessible Island.

earthquakes between the MAR and TdC. This band of events is interrupted by a circular area devoid of seismicity southwest of the island with an east-west extent of ~ 200 km and a north-south extent of ~ 100 km (marked in Figure 4). We also observe earthquakes in close proximity to the archipelago. These events are arranged in three distinct clusters (Figure 5). We detected no earthquakes east of 11.5°W. The corresponding error ellipses of the 2012 events are in most cases smaller than the plotted location dots in the map (Figure S4).

In detail, the region north of the NFZ (from 36°S to 34°S) shows a high level of seismicity, along the transform faults and fracture zones and intraplate east of the MAR. Farther north, we locate most of the earthquakes along a transform fault at ~ 32.5°S and only a few intraplate earthquakes east of the MAR (from 33.5°S to 32.5°S). Apart from a few individual outliers (located on a fracture zone at ~ 34°S or at 16.26°W and 34.84°S), the error ellipses of these events are small (compare Figure S4a with Figure S4b). The large uncertainties of the outliers allow different locations shifted on a line directed either toward or away from the center of the network, but a location in close proximity to a NEIC catalog earthquake or on a fracture zone is the most probable source locations. We detect earthquakes in the farthest north only at magnitudes exceeding 4 due to large source-receiver distances.

Surprisingly, intraplate seismicity dominates the central Tristan Segment (TS). The earthquakes occur between 16°W and 13°W approximately 120 km to 380 km east of the active spreading MAR with local magnitudes between 3 and 4. The small error ellipses of these events (Figure S4b) clearly indicate intraplate locations. The magnitudes increase toward the NNW away from TdC, reaching 4.8 near the segment-bordering northern fracture zone (NFZ). The NFZ is characterized by many earthquakes with magnitudes larger than 4. Only a few events were located along the MAR.

Significant seismicity (events with local magnitudes of 2.5 to 3.5) can be observed in the STS within a band running from the TdCFZ toward the SFZ between 15°W and 13°W. We detect several earthquakes at the TdCFZ west of 14°W with local magnitudes ranging between 3 and 4 and from 12.5°W to 11.5°W with magnitudes 2 to 3. Further earthquakes occur at the SFZ between 16°W and 13°W and a few along the MAR. The error ellipses of these intraplate earthquakes are small. Earthquakes south of 39.5°S have large major axes lengths, again directed toward the center of the network, but these uncertain locations are irrelevant for our interpretation.

It was quite unexpected that we do not locate any events in an area slightly west and southwest of the archipelago (marked in Figure 4). Small error ellipses of earthquakes adjoining this area eliminate a mislocation. But we observed earthquakes close to the TdC islands and seamounts (Figure 5). It is apparent that these events are arranged in distinct clusters. Cluster c1 is positioned northwest of Inaccessible Island (37°S, 13.4°W, Figure 5a). Here we detected more than 10 earthquakes with magnitudes between 2.2 and 3.3. The corresponding error ellipses are again smaller than the plotted dots (Figure 5a). Two other earthquake clusters (c2 and c3) can be observed close to the TdCFZ between 12.5°W and 11.5°W but farther east (east of 12.5°W) of its above mentioned main zone of activity (16°W to 14°W). Cluster c2 is located directly southeast of Nightingale Island (12.8°W to 12°W, ML: 2–3), and cluster c3 is positioned farther to the east near 37.7°S, 11.5°W. Because these 20 earthquakes are located within our network and prominent *P* and *S* wave arrivals are visible, the error ellipses of c2 and c3 are very small (Figure 5a) and we were able to determine hypocenter depths (Figure 5b). The depths range mostly between 20 km and 30 km (depth errors ~ 3 km). We associated a NEIC earthquake location of the year 2013 to cluster c3 and the NEIC location of the large 2004 event

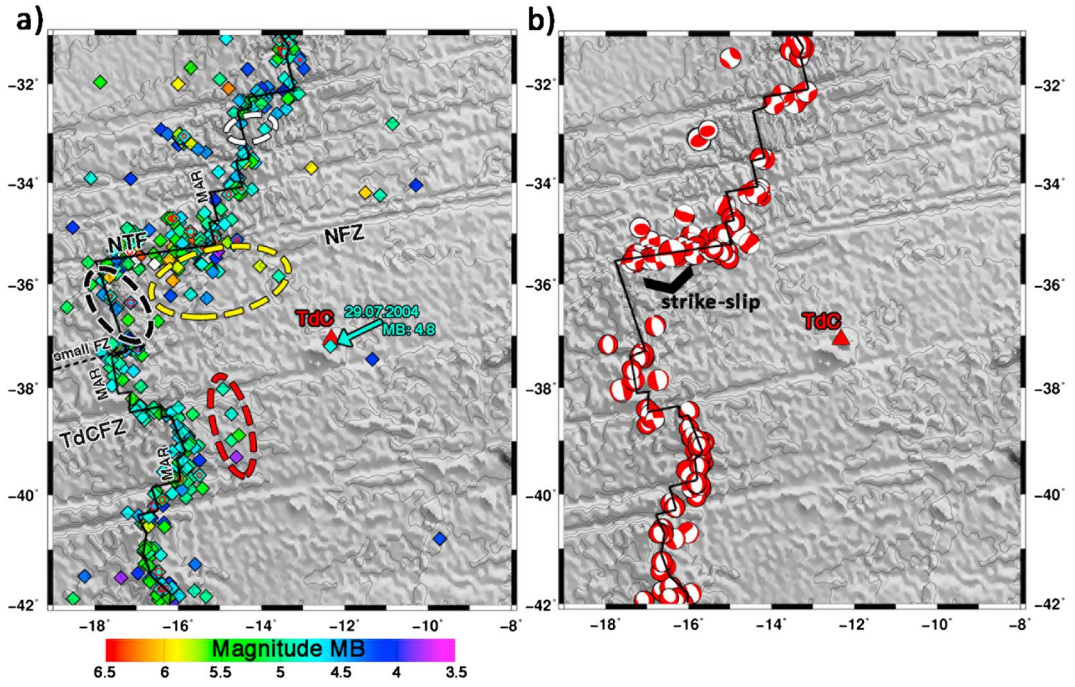

Figure 6. (a) Locations of NEIC earthquakes from 1968 to 01.08.2016. The color indicates the body wave magnitude MB. The cyan arrow marks the 2004 earthquake (MB: 4.8). Red dashed line, intraplate seismicity east of the MAR. Black dashed line, zone of low on-axis seismicity. Yellow dashed line, intraplate seismicity south of the NFZ. White dashed line, a second aseismic on-axis seismicity. Earthquakes after 2014 show horizontal uncertainties (red circles). (b) Focal mechanism solutions from the Harvard CMT catalog (1968–01.08.2016).

northeast of Nightingale Island to cluster c2 (Figures 5a and 6a). O'Mongain et al. (2007) localized a swarm of earthquakes at the same day, which we also relate to c2 (Figure 5a).

4.2. Temporal Distribution of Earthquakes

In order to recognize temporal patterns in seismicity, we plotted the number of local earthquakes for each day in 2012 (Figure 7a). Only a few earthquakes could be evaluated between June and August, owing to masking of their *P* wave arrivals by whale vocalizations. Spatial clusters of more than four earthquakes are mostly confined to a single day and a relatively small region (Figure 7c). We observed a temporal and geographical north-south movement of earthquakes at two specific days (Figure 7c, red and blue frames). Events per day for NTS, TS, and STS are provided in Figure S3 of the supporting information.

4.3. Comparison With Long-Term Seismicity

To place our observations in the context of long-term seismicity, we present the available NEIC earthquake locations and their related body wave magnitudes (MB) for the time period May 1969 to July 2017 (Figure 6a). The catalog did not provide location uncertainties before the year 2014, but we conclude that these locations have large location errors due to the scarcity of permanent installed seismometers in the study area. The seismometer station on TdC is operated only since 2004 and the next seismometer station on St. Helena is 1,560 km away. In most cases the provided horizontal uncertainties since 2014 are smaller than 15 km (Figure 6a). The catalog event locations are mostly confined to the axis of the MAR, but some deviations from the axis are visible and coincide with our earthquake locations of 2012. A few events have a sufficient distance to the NFZ to be clearly classified as intraplate earthquakes (Figure 6a, yellow dashed line) and can therefore be compared to our observations (see section 4.1 and Figure 4). Five of the cataloged earthquakes occurred within the STS along a ridge-parallel band running southward from the TdCFZ at 14.8°W toward the SFZ (Figure 6a, red dashed line). This band also coincides with a region of high seismicity within the STS in our local observations. Fewer than eight events occurred along the MAR at latitudes between 37°S and 36°S (Figure 6a, black dashed line). Our results show a similar lack of seismicity at

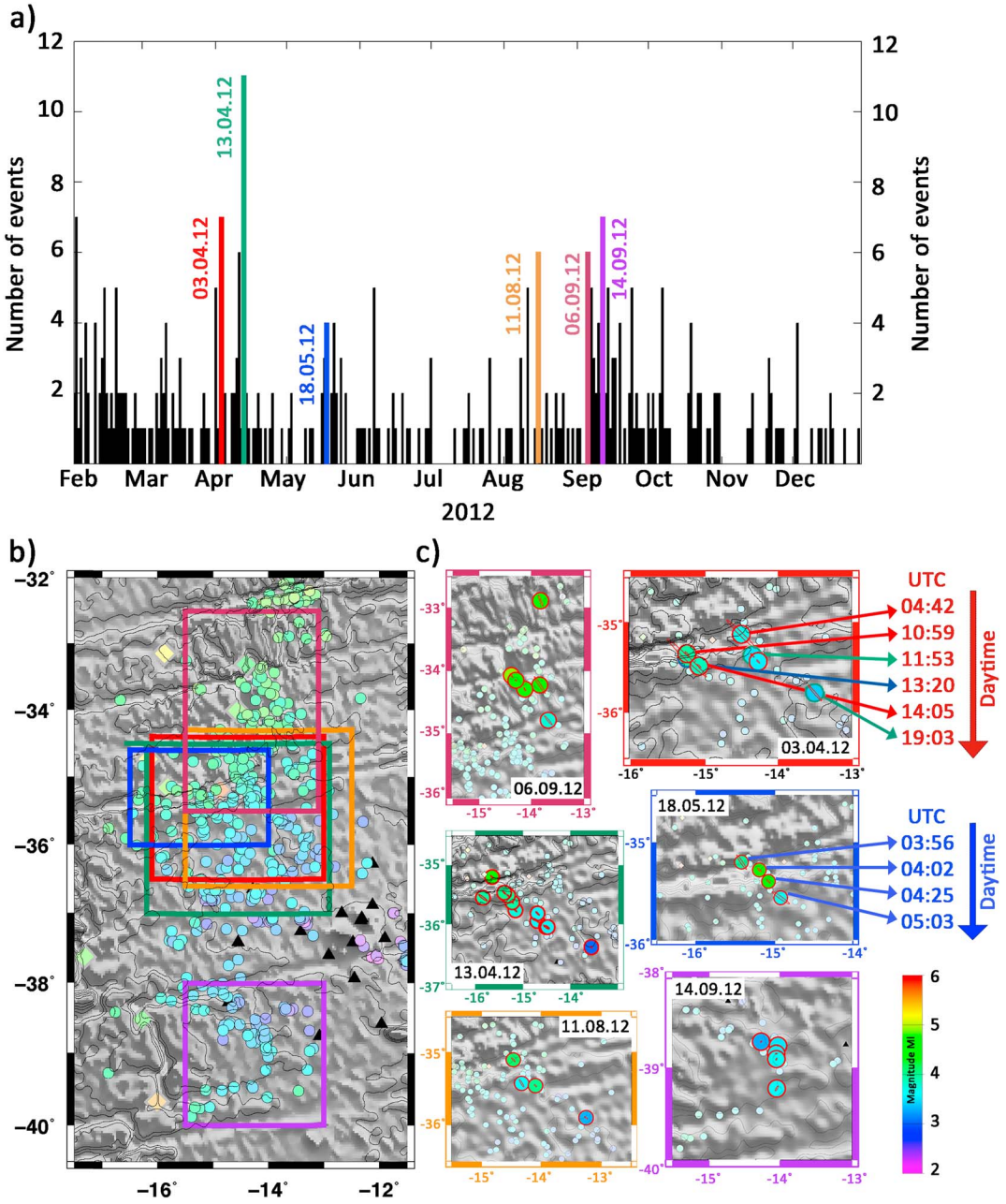

Figure 7. (a) Number of earthquakes per day. The specific days focused in Figure 7c are color indicated. (b) Color marked regions focused in Figure 7c. (c) Earthquakes at specific days with its error ellipses. At 2 days (03.04.2012, 18.05.2012) the earthquakes are labeled with their origin time.

this segment of the MAR crest. The ridge segment between 34°S and 33°S shows a similar paucity of seismicity (Figure 6a, white dashed line). To the west of this segment, the NEIC locations show some intraplate earthquakes aligned northwest to southeast between 17°W and 15°W. (Two focal mechanism solutions are available for these events (Figure 6b).) We located two earthquakes in the same region in 2012 (Figure 4).

Unfortunately, the Harvard CMT (Centroid Moment Tensor) catalog provides only focal mechanisms of earthquakes at the axis of MAR and transforms faults (Figure 6b) and no intraplate events, which could be of interest for our study. The data of the catalog show a typical strike-slip source mechanism at the transform fault along the NFZ and a typical normal fault mechanism at the mid-Atlantic spreading ridge (Figure 6b).

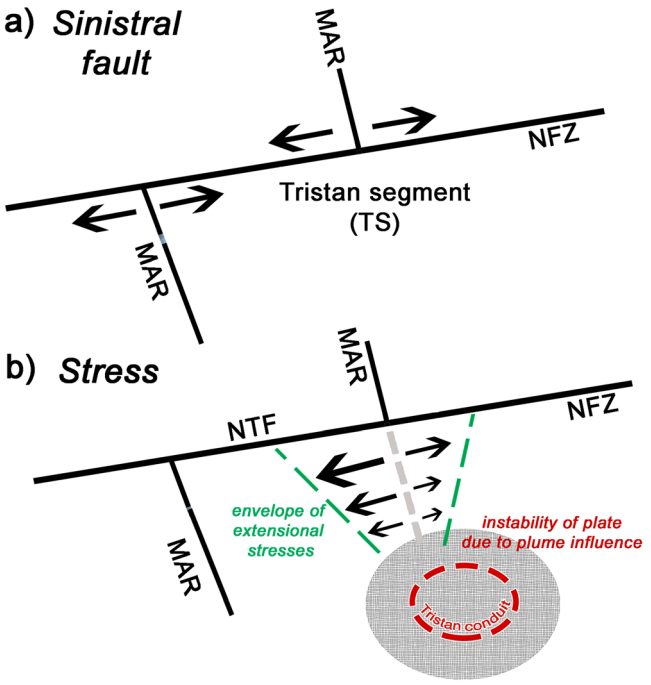

Figure 8. (a) Directions of relative motion of the Tristan Segment (TS) and its bordering segments. (b) The arrows indicate the extensional stresses within the TS. The green dashed line marks their envelope. This schematic display is derived from a picture published by Van Wijk and Blackman (2005), showing the extensional forces σ_{xx}, calculated for a 100 km transform fault. The red dashed ellipse marks the Tristan plume location published by Schlömer et al. (2017), and the gray ellipse marks the area, where the plume influences the plate rheology.

A comparison between the 2012 NEIC locations and our locations (Figure S5) shows accordance and also a few differences. Locations along the NFZ and at the MAR crest south of the NFZ show a good correlation apart from a significant difference between locations at the SFZ. Our locations north of 34.8°S are shifted toward the center network in comparison to the NEIC locations. The greater the source-network distance, the greater the shift between the locations. This effect is typical for locations outside local networks. The magnitude differences (ML-MB) are in most cases smaller than 0.3 (Table S4).

5. Interpretation and Discussion

5.1. Intraplate Seismicity: Plate Tectonics and Plume Existence

We observe numerous earthquakes with magnitudes 3.5–4 at the large Northern Transform Fault (Figure 4). Here the plate boundaries move horizontally and past each other on strike-slip faults (Figures 8a and 6b). The repeated rupture of brittle rocks along the transform fault generates these earthquakes. The plate segments are hooked together at their borders, and the movement in opposite directions causes extensional stress within the TS (Figure 8b). At the eastern end of the transform fault on the NFZ, cold lithosphere of the TS juxtaposes against a hot ridge axis. A bulge is developed on the cold side of the fault by intrusions of hot dikes or conductive heating from the hot ridge. These lithospheric differences in addition to the tectonic setting cause extensional stresses at the end of the ridge crest in the TS. Van Wijk and Blackman (2005) investigated the deformation of oceanic lithosphere at a 100 km transform fault and found out that the extensional stresses concentrate in an area about several tens of kilometers in a line with the ridge tip in the older plate (Figure 8b). Therefore, we associate the significant occurrence of intraplate earthquakes south of the NFZ to these extensional stresses. Since extensional stress decreases with increasing distance from the transform fault, we would expect a decreasing and finally disappearing seismicity south of the ridge tips in the TS. But in contrast to this we observe intraplate seismicity passing throughout the TS, lacking in an area southwest of TdC and running farther throughout the STS (Figure 4). We think that the Tristan mantle plume (Schlömer et al., 2017) in the southern part of the TS causes a rheological weakening of the plate (Figure 8b). Cold lithosphere in the northern and southern STS in contrast to the hotter lithosphere in the plume region might create a thermal stress field. These stresses are reflected by the significant persistent intraplate seismicity within the segments.

Earthquakes can be triggered by changes in stress (e.g., Stein, 1999) or by fluid intrusion (e.g., Nur & Booker, 1972). Hainzl (2004) investigated an earthquake swarm in the Vogtland/W-Bohemia region and revealed that stress triggering dominates after a fault patch has been brought into a critical state by an increase in pore pressure. Therefore, we assume that the tectonic stresses caused the seismicity in close vicinity to the NTF, while the influence of magmatic fluids cannot be ruled out farther south in the TS, close to the Tristan plume conduit. As a consequence of this, we think that we are able to identify a temporal propagation of stresses by observations of two event clusters on two separate days. First, accumulated stress at the NTF is released by a strike-slip earthquake (initial main shock). The corresponding plate movement lead to the development of a drag force at the northwestern boundary of the TS and the propagation of extensional forces southward through the TS (Figure 8b). The first earthquake of each day occurred at the NFZ (Figure 7b, red and blue maps). In response to the plate movement, we observe intraplate earthquakes that propagate into the plate interior and reflect the extensional stresses later in each of the 2 days (aftershocks). The southwest propagation of earthquakes follows the envelope of extensional stresses in an area south of the ridge tips (Figure 8b derived from Van Wijk & Blackman, 2005).

To summarize, the spatial and temporal distribution of intraplate earthquakes reflects the prevailing stress field, which is strongly influenced by the special tectonic setting (among others the large transform fault in

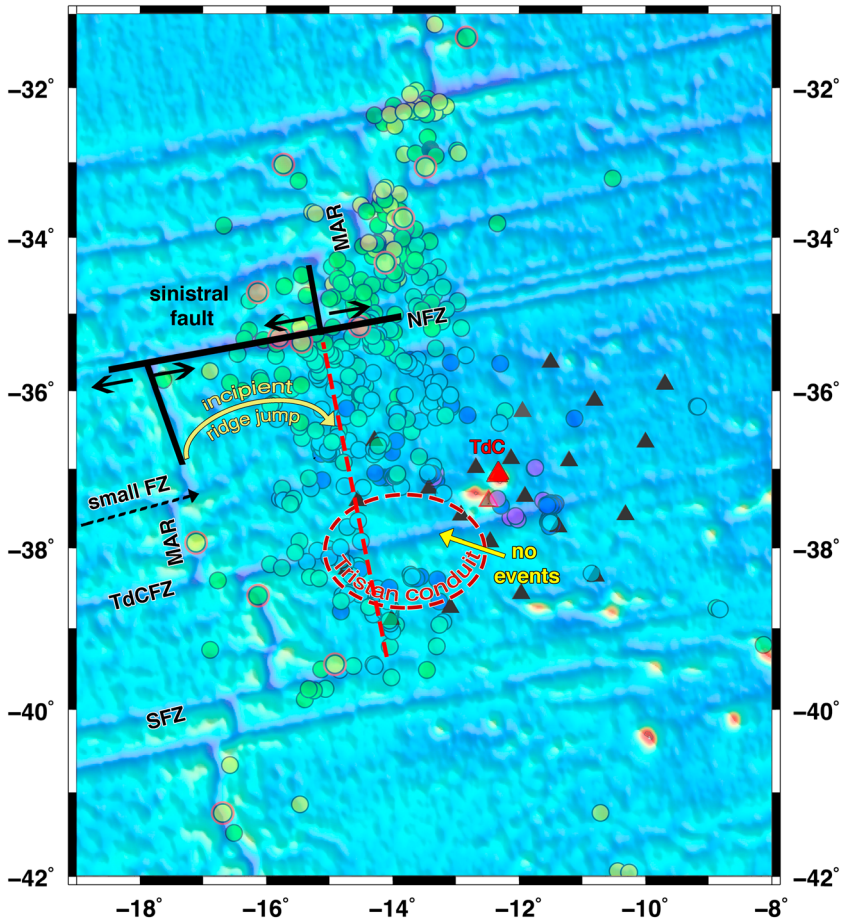

Figure 9. Overview map with main interpretations: Border of the Tristan da Cunha conduit (Schlömer et al., 2017) coincides with an aseismic area. Sinistral fault mechanism at the plate segment north of TdC. Zone of intraplate seismicity (red dashed line), interrupted by the Tristan conduit and continuing in the STS represents a weakening of the involved plate segments and might be the new location for an incipient ridge jump. Abbreviations are listed in Figure 1.

the north), surrounding the seismological network and the Tristan mantle plume beneath the network. We do not compare our results with other studies investigating intraplate seismicity near ridges (e.g., Bergman & Solomon, 1984; Stein et al., 1987), since the tectonic setting in the Tristan region is unique. In most studies at MAR the seismological networks are arranged on the ridge axes or transform faults and not intentionally a few hundred kilometers away from them.

5.2. Regions of No Seismicity

Southwest of TdC we observe a significant elliptical region that lacks seismicity. Since earthquakes are generated by brittle failure of rocks, the increased presence of melt, with its high viscosity, and the related absence of frictional forces could explain the lack of seismicity. Overlapping Figures 1 and 4, it seems that the aseismic region is confined to the eastern part of the Tristan conduit as defined by Schlömer et al. (2017) (Figure 9). This aseismic region is surrounded by earthquakes (Figure 4). Besides the presence of melt that this might indicate, the tomography images also hot temperatures, while earthquakes indicate failures of rocks. Therefore, the aseismic/seismic border may indicate the transition zone between ductile (reheated lithosphere by the underlying plume) and the surrounding brittle regime. Besides elevated temperatures the aseismic zone could potentially indicate weakening of the lithosphere by ascending fluids. Further investigations of the seafloor in this area are necessary to confirm potential magmatic activity there.

The catalog of long-term observations and our observations in 2012 reveal infrequent seismicity along the MAR crest (Figures 6 and 4). This coincidence indicates a persistent lack of seismicity at time scales of at

least a few decades and excludes that the aseismic regions can be assigned to a variable temporal characteristic. Since the lithosphere along or near the ocean ridge crest is hot and ductile in comparison to old, cool, and therefore more brittle lithosphere at the transform faults, most of the higher-magnitude earthquakes occur on transform offsets rather than on the ridge crest itself. Many previous studies reported also on seismically inactive regions along the Mid-Atlantic ridge axis (e.g., Barclay, Toomey, & Solomon, 2001; Smith et al., 2003; Tilmann et al., 2004; Wolfe et al., 1995). Since this topic is not the main theme of this article, we will not go into further details here.

On the basis of the large transform fault, cold lithosphere of the TS juxtaposes against the hot ridge axis at the eastern end of the NTF. Furlong et al. (2001) suggested that the presence of older and thicker lithosphere from opposite of the ridge axis might eventually result in the formation of a new, short ridge segment. In extension of the ridge axis, the strong extensional stress field in the TS weakens the lithosphere. Furthermore, the lithosphere is reheated by magma originating from the Tristan conduit and thus, potentially, thermally thinned by the underlying plume. These processes may indicate a tendency for the MAR to relocate eastward (Figure 9). A few authors already predicted jumps of the MAR segment toward the Tristan da Cunha hot spot (e.g., Briais & Rabinowicz, 2002; Mittelstaedt et al., 2008). In a first instance, the relocation of the MAR axis would stop the slip movement of the TS and the bordering NTS. But a recently large earthquake at the NTF (Origin time: 17.06.2015 12:51:32 UTC, 35.36°S and 17.16°W, MB: 7) and continuous seismicity along the NFZ argue against an entire ridge jump. Further investigations concerning this topic are necessary to assess a theory.

5.3. Earthquakes Close to the Archipelago of TdC

Earthquakes close to the archipelago of TdC are distributed in different earthquake clusters (c1–c3). Two hypocenter locations of the 2012 events coincide spatially with the swarm of earthquakes in 2004, and three earthquakes occurred slightly farther south at the TdCFZ (Figure 5a, c2). Our most eastern earthquake cluster (c3) coincides also with a 2013 NEIC earthquake. Therefore, we assume long-term activities in these regions. This answers the question raised by O'Mongain et al. (2007) whether the July 2004 swarm, including the large NEIC earthquake with its abrupt onset, can be considered as an isolated event or as part of a history of ongoing regular activity.

So far, the causes of this seismicity (c2) have only been speculative. Geissler et al. (personal communication) discovered a new submarine volcano, named Isolde, at the flanks of Nightingale Island during the cruise MSM 20/2 (Figure 5a, magenta cross). The peak of Isolde is situated ~ 300 m below the sea surface in a seismically active region. The authors proposed that the Isolde seamount might be the location of the vent responsible for the 2004 eruption. The occurrence of earthquakes 8 years later could indicate ongoing tectono-magmatic activity in that area.

An additional earthquake cluster (c1) can be observed west/northwest of Inaccessible Island (Figure 5a). This cluster coincides with Geissler et al.'s (personal communication) interpretation of monogenetic volcanic fields in bathymetry and sediment echosounder data (Figure 5a, marked with red dashed lines). The correlation suggests farther area of recent volcanic or intrusive activity. The occurrence of earthquakes in different clusters (c1–c3) in addition with the recent discovery of the Isolde seamount and new volcanic fields supports the theory of Schlömer et al. (2017) that material is channeled from the Tristan plume to specific locations at the seafloor. Ryberg et al. (2017) recently analyzed ambient seismic noise around TdC and derived a 3-D *S* wave velocity model. Their velocity structure also indicates a magmatic feeding system beneath the archipelago.

Moreover, it has been presumed that transform faults and fracture zones not only are topographic features but also influence the underlying lithosphere. Ryberg et al. (2017) illustrated that the TdCFZ can be traced seismically into the uppermost mantle and Schlömer et al. (2017) proposed that topography at the base of the lithosphere at this fracture zone controls the melting within the uprising plume material. We therefore relate earthquakes at the TdCFZ (c2 and c3) at depths ranging from 20 km to 30 km to the upper mantle structure influenced by the overlying transform fault.

Ongoing local seismic monitoring with higher station density and the ability of a precise localization in addition to high-resolution bathymetric data are necessary to make further statements on the seismic activity and accompanying seismic or volcanic hazard of the TdC region.

6. Conclusions

This study allows a unique insight into the poorly known and rarely investigated tectonic and magmatic processes in the Tristan da Cunha region. A temporarily seismological network consisting of ocean-bottom seismometers and land station, surrounding the archipelago of Tristan da Cunha, was used to register and locate local earthquakes. Unexpected high seismicity is observed within the segment of the African plate north of Tristan da Cunha. We relate this to extensional stresses caused by the tectonic setting at the northern boundary of this plate segment and to the existence of the Tristan mantle plume beneath its southern boundary. The reheated lithosphere above the plume destabilizes the plate segment and causes stresses. The chronological sequence of events and their magnitudes points to linked processes at and within plate segments: While plate motion triggers large earthquakes at the transform fault, the bordering segments undergo stretching that leads to extensional intraplate earthquakes. The extensional stresses in addition to the thermally thinning of the lithosphere by the mantle plume weaken the plate segment. The associated intraplate earthquakes might indicate an incipient eastward ridge jump.

An area without seismicity southwest of the archipelago coincides spatially with the proposed location of the Tristan conduit. We relate the absence of earthquakes to a reheated lithosphere and define the margins of the aseismic/seismic zone to the transition between brittle and ductile regime. We located earthquakes in close vicinity to the archipelago and nearby seamounts, which hint to ongoing tectono-magmatic activity in the Tristan da Cunha area.

Acknowledgments
We thank the DFG (Deutsche Forschungsgemeinschaft) and "Senatskomission für Ozeanographie" for funding SAMPLE (South Atlantic Margin Processes and Links with onshore Evolution) Priority Program 1375 (JE296/9-1, GE 1783/4-2). Also, we thank the master Ralf Schmidt and the crew of Maria S. Merian. We thank the DEPAS (Deutsche Geräte-Pool für amphibische Seismologie) instrument pool and the BGR (Bundesanstalt für Geowissenschaften und Rohstoffe) for providing us data from the IMS's 11 of the CTBTO. Furthermore, we thank anonymous reviewers for their constructive criticism. The data used for this study are archived at Alfred Wegener Institute (www.awi.de) and can be requested from wolfram.geissler@awi.de.

References

Anderson, D. L., & Schramm, K. A. (2005). Global hotspot maps. *Special Papers-Geological Society of America*, *388*, 19.

Baker, P. E., Gass, I., Harris, P., & le Maitre, R. (1962). The volcanological report of the Royal Society Expedition to Tristan da Cunha. *Philosophical Transactions of the Royal Society of London*, 256.

Barclay, A. H., Toomey, D. R., & Solomon, S. C. (2001). Microearthquaks characteristics and crustal V_p/V_s structure at the Mid-Atlantic Ridge, 35°N. *Journal of Geophysical Research*, *106*(B2), 2017–2034. https://doi.org/10.1029/2000JB900371

Bergman, E. A., & Solomon, S. C. (1984). Source mechanisms of earthquakes near mid-ocean ridges from body waveform Inversion: Implications for the early evolution of oceanic lithosphere. *Journal of Geophysical Research: Solid Earth*, *89*(B13), 11,415–11,441. https://doi.org/10.1029/JB089iB13p11415

Briais, A., & Rabinowicz, M. (2002). Temporal variations of the segmentation of slow to intermediate spreading mid-ocean ridges 1. Synoptic observations based on satellite altimetry data. *Journal of Geophysical Research: Solid Earth*, *107*(B5), 2098. https://doi.org/10.1029/2001JB000533

Courtillot, V., Davaille, A., Besse, J., & Stock, J. (2003). Three distinct types of hotspots in the Earth's mantle. *Earth and Planetary Science Letters*, *205*(3-4), 295–308. https://doi.org/10.1016/S0012-821X(02)01048-8

Furlong, K. P., Sheaffer, S. D., & Malservisi, R. (2001). Thermal rheological controls on deformation within oceanic transforms. *Geological Society London, Special Publications*, *186*, 65–83.

Geissler, W. H., Jokat, W., Jegen, M., & Baba, K. (2016). Thickness of the oceanic crust, the lithosphere, and the mantle transition zone in the vicinity of the Tristan da Cunha hot spot estimated from ocean-bottom and ocean-island seismometer receiver functions. *Tectonophysics*, *716*, 35–51.

Hainzl, S. (2004). Seismicity patterns of earthquake swarms due to fluid intrusion and stress triggering. *Geophysical Journal International*, *159*, 1090–1096. https://doi.org/10.1111/j.1365-246X.2004.02463.x

Hards, V. (2004). Assessment of volcanic activity in the wake of the seismic episode of 29/30 July 2004 on Tristan da Cunha, South Atlantic Ocean. *British Geological Survey Commissioned Report CR/04/235*.

Haxel, J., & Dziak, R. (2005). Evidence of explosive seafloor volcanic activity from the Walvis Ridge, South Atlantic Ocean. *Geophysical Research Letters*, *32*, L13609. https://doi.org/10.1029/2005GL023205

Jokat, W., & Reents, S. (2016). Hotspot volcanism in the southern South Atlantic: Geophysical constraints on the evolution of the southern Walvis Ridge and the Discovery Seamounts. *Tectonophysics*, *716*, 77–89.

Mittelstaedt, E., Ito, G., & Behn, M. D. (2008). Mid-ocean ridge jumps associated with hotspot magmatism. *Earth and Planetary Science Letters*, *266*, 256–270. https://doi.org/10.1016/j.epsl.2007.10.055

Morgan, W. J. (1971). Convection plumes in the lower mantle. *Nature*, *230*(5288), 42–43. https://doi.org/10.1038/230042a0

Nur, A., & Booker, J. R. (1972). Aftershocks caused by pore fluid flow? *Science*, *175*(4024), 885–887. https://doi.org/10.1126/science.175.4024.885

O'Connor, J., & Duncan, R. (1990). Evolution of the Walvis Ridge-Rio Grande Rise hot spot system: Implications for African and South American plate motions over plumes. *Journal of Geophysical Research*, *95*(B11), 17,475–17,502. https://doi.org/10.1029/JB095iB11p17475

O'Mongain, A., Ottemoller, L., Baptie, B., Galloway, D., & Booth, D. (2007). Seismic activity associated with a probable submarine eruption near Tristan da Cunha, July 2004–July 2006. *Seismological Research Letters*, *78*, 375–382. https://doi.org/10.1785/gssrl.78.3.375

Pavlis, G. L., Vernon, F., Harvey, D., & Quinlan, D. (2004). The generalized earthquake-location (GENLOC) package: An earthquake-location library. *Computers & Geosciences*, *30*, 1079–1091. https://doi.org/10.1016/j.cageo.2004.06.010

Rohde, J. K., van den Bogaard, P., Hoernle, K., Hauff, F., & Werner, R. (2013). Evidence for an age progression along the Tristan-Gough volcanic track from new $^{40}Ar/^{39}Ar$ ages on phenocryst phases. *Tectonophysics*, *604*, 60–71. https://doi.org/10.1016/j.tecto.2012.08.026

Ryberg, T., Geissler, W., Jokat, W., & Pandey, S. (2017). Uppermost mantle and crustal structure at Tristan da Cunha derived from ambient seismic noise. *Earth and Planetary Science Letters*, *471*, 117–124. https://doi.org/10.1016/j.epsl.2017.04.049

Sandwell, D. T., Müller, R. D., Smith, W. H., Garcia, E., & Francis, R. (2014). New global marine gravity model from CryoSat-2 and Jason-1 reveals buried tectonic structure. *Science*, *346*(6205), 65–67. https://doi.org/10.1126/science.1258213

Schlömer, A., Geissler, W. H., Jokat, W., & Jegen, M. (2017). Hunting for the Tristan mantle plume—An upper mantle tomography around the volcanic island of Tristan da Cunha. *Earth and Planetary Science Letters*, *462*, 122–131. https://doi.org/10.1016/j.epsl.2016.12.028

Smith, D. K., Escartin, J., Cannat, M., Tolstoy, M., Fox, C. G., Bohnenstiehl, D. R., & Bazin, S. (2003). Spatial and temporal distribution of seismicity along the northern Mid-Atlantic Ridge (15°–35°N). *Journal of Geophysical Research: Solid Earth*, *108*(B3), 2167. https://doi.org/10.1029/2002JB001964

Stein, R. S. (1999). The role of stress transfer in earthquake occurrence. *Nature*, *402*(6762), 605–609. https://doi.org/10.1038/45144

Stein, S., Cloetingh, S., Wiens, D. A., & Wortel, R. (1987). Why does near ridge extensional seismicity occur primarily in the Indian Ocean? *Earth and Planetary Science Letters*, *82*(1-2), 107–113. https://doi.org/10.1016/0012-821X(87)90110-5

Tilmann, F., Flueh, E., Planert, L., Reston, T., & Weinrebe, W. (2004). Microearthquake seismicity of the Mid-Atlantic Ridge at 5 S: A view of tectonic extension. *Journal of Geophysical Research: Solid Earth*, *109*, B06102. https://doi.org/10.1029/2003JB002827

Van Wijk, J., & Blackman, D. (2005). Deformation of oceanic lithosphere near slow-spreading ridge discontinuities. *Tectonophysics*, *407*, 211–225. https://doi.org/10.1016/j.tecto.2005.08.009

Wadati, K., & Oki, S. (1933). On the travel time of earthquake waves (Part II). *Journal of the Meteorological Society of Japan. Ser. II*, *11*(1), 14–28. https://doi.org/10.2151/jmsj1923.11.1_14

White, R., & McKenzie, D. (1989). Magmatism at rift zones: The generation of volcanic continental margins and flood basalts. *Journal of Geophysical Research: Solid Earth*, *94*(B6), 7685–7729. https://doi.org/10.1029/JB094iB06p07685

Wolfe, C. J., Purdy, G., Toomey, D. R., & Solomon, S. C. (1995). Microearthquake characteristics and crustal velocity structure at 29°N on the Mid-Atlantic Ridge: The architecture of a slow spreading segment. *Journal of Geophysical Research: Solid Earth*, *100*(B12), 24,449–24,472. https://doi.org/10.1029/95JB02399